Bioactive Materials 6 (2021) 4333–4341

Contents lists available at ScienceDirect

Bioactive Materials

journal homepage: www.sciencedirect.com/journal/bioactive-materials

A novel lean alloy of biodegradable Mg–2Zn with nanograins

Wenhui Wang [a,b], Carsten Blawert [b], Rui Zan [a], Yu Sun [a], Hongzhou Peng [a], Jiahua Ni [c,**], Pei Han [d], Tao Suo [e], Yang Song [a], Shaoxiang Zhang [f,***], Mikhail L. Zheludkevich [b,****], Xiaonong Zhang [a,*]

[a] State Key Laboratory of Metal Matrix Composites, School of Materials Science and Engineering, Shanghai Jiao Tong University, Shanghai, 200240, China
[b] Magnesium Innovation Centre (MagIC), Institute of Materials Research, Helmholtz-Zentrum Geesthacht, Geesthacht, 21502, Germany
[c] Department of Mechanical Engineering, Massachusetts Institute of Technology, Cambridge, MA, 02139, United States
[d] Orthopaedic Department, Shanghai Jiao Tong University Affiliated Sixth People's Hospital, Shanghai, 200233, China
[e] Zhongshan Hospital Fudan University, Shanghai, 200233, China
[f] Suzhou Origin Medical Technology Co. Ltd., Jiangsu, 215513, China

ARTICLE INFO

Keywords:
Magnesium alloy
Nanocrystal
Biodegradable
Rolling
Microstructure

ABSTRACT

Lean alloy (low alloyed) is beneficial for long-term sustainable development of metal materials. Creating a nanocrystalline microstructure is a desirable approach to improve biodegradability and mechanical properties of lean biomedical Mg alloy, but it is nearly impossible to realize. In the present study, the bulk nanocrystalline Mg alloy (average grain size: ~70 nm) was successfully obtained by hot rolling process of a lean Mg-2wt.%Zn (Z2) alloy and both high strength ((223 MPa (YS) and 260 MPa (UTS)) and good corrosion resistance (corrosion rate in vivo: 0.2 mm/year) could be achieved. The microstructure evolution during the rolling process was analyzed and discussed. Several factors including large strain, fine grains, strong basal texture, high temperature and Zn segregation conjointly provided the possibility for the activation of pyramidal <c+a> slip to produce nanocrystals. This finding could provide a new development direction and field of application for lean biomedical Mg alloys.

1. Introduction

Magnesium (Mg), a biodegradable metal, is a promising material for degradable implant devices due to excellent mechanical compatibility to bone [1], superior biocompatibility [2], and special bio-functions [3], which have been researched and developed for more than ten years. Even though traditional alloying method still dominats the development of biomedical Mg to achieve high performance (high strength and low corrosion rate), low alloy systerms (lean alloy) have a better perspective for long-term sustainable development, because it can simplify their processing including recycling, and avoid the risk of exhaustion of rare elements (RE) [4,5]. Anyway, decreasing or forbidding adverse elements such as Al and RE is an option, thus microalloying can ensure the biosafety [6]. However, the mechanical properties of Mg mainly depend on the strengthening effects of the alloying elements, especially precipitation strengthening [7]. With limited number of alloying elements, controlling microstructure is the primary way to maintain properties.

Nanocrystalline metals (grain size <100 nm) contain a large fraction of grain boundaries (GBs), usually showing superior strength according to the Hall-Petch relation [8,9]. Moreover, grain refinement and surface nanocrystalline can improve the corrosion resistance of Mg alloys [10]. Nanostructured material can also influence the behaviour of cell proliferation and differentiation [11]. Therefore, it is a practical way to obtain high strength and improve corrosion resistance by nanocrystalline Mg alloys.

However, bulk nanocrystalline Mg alloys have not been reported in

Peer review under responsibility of KeAi Communications Co., Ltd.
* Corresponding author.
** Corresponding author.
*** Corresponding author.
**** Corresponding author.
E-mail addresses: nijiahua2012@gmail.com (J. Ni), sxzhang@originmedtech.com (S. Zhang), Mikhail.L.Zheludkevich@hzg.de (M.L. Zheludkevich), xnzhang@sjtu.edu.cn (X. Zhang).

https://doi.org/10.1016/j.bioactmat.2021.04.020
Received 20 December 2020; Received in revised form 8 April 2021; Accepted 12 April 2021

literatures before. Until now, just bulk ultra-fine-grained Mg alloys (100 nm~1 μm) were successfully processed by using sophisticated severe plastic deformation (SPD) technologies. For example, the grains size was 340 nm in WE43 magnesium alloy processed by ECAP [12] and 500 nm in AZ31 magnesium alloy processed by high-pressure torsion [13]. Mg with hexagonal close packing (hcp) crystal structure is challenging to provide large deformations at relatively low temperatures [14]. Interestingly, in the present work the bulk nanocrystalline Mg–2Zn (Z2) binary alloy with high strength, and favourable corrosion resistance was produced by hot rolling process. The Z2 alloy contains only nutritive element, which has shown in vitro and in vivo studies to have superior biosafety [15,16]. The present study characterizes the microstructures of Z2 alloy and discusses the mechanism of grain refinement during rolling process. This work is not only providing a practical approach to realize a new lean biodegradable Mg alloy but also contributes to the development of nanocrystalline Mg alloys.

2. Materials and methods

2.1. Material processing

The as-cast ingots of Z2 alloy were provided by Suzhou Origin Medical Technology Co. Ltd., China. The chemical composition of Z2 could be found in Table 1. A rectangular plate 50 (RD) × 50 (TD) × 22 (ND) mm was cut from the ingot for hot rolling (where RD is the rolling direction, TD the transverse direction and ND the normal direction). The samples were hot-rolled at 400 °C with a reduction of 20% and 50% in one pass, named as R1-20% and R1-50% respectively. The second pass was 50% rolling reduction acted on R1-50%, named as R2-75%. The third pass was 64% rolling reduction acted on R2-75%, named as R3-91% with the final thickness of 2 mm. All samples were reheated at 400 °C for 5min between every two contiguous passes. The diameter of the rolls was 160 mm, and the rolling speed was 14 m/min.

2.2. Microstructural analysis

The specimen for determination of the microstructure of rolled samples was cut from the core of rolled sheets and characterized by Electron Backscatter Diffraction (EBSD) measurements performed with a scanning electron microscope (Mira3 (SEM) & AZtec Nordlys Max3). The EBSD data was analyzed by Channel 5 analysis software. Specimens for EBSD measurements were prepared by conventional grinding and diamond polishing (down to 0.5 μm), followed by Ar^+ ion milling in a precision ion polishing system (PIPS, Gatan). The accelerating voltage in operation is 0.5 kV, and the incident angle was set at 3° under a liquid-nitrogen cooling system. For transmission electron microscopy (TEM), thin foil specimens were prepared by punching 3 mm diameter discs, followed by dimple grinding and Ar^+ ion milling in the precision ion polishing system. The accelerating voltage in operation was 4.5 kV, and the incident angle was set at 6°. High angle annular dark-field (HAADF)-scanning transmission electron microscopy (STEM), and annular dark field (SDF) STEM images were obtained using a FEI Talos-F200X (200 kV) equipped with a field-emission gun. Corrosion morphology were characterized through a scanning electron microscope with energy dispersive spectroscopy (TESCAN-RISE).

2.3. Tensile testing

Tensile testing samples were cut from the rolled sheets with a gauge length of 10 mm, a width of 4 mm, and a thickness of 2 mm. They were tested using a SANS type tensile test machine. The tensile direction was along the RD of the samples, and the test was conducted with a strain rate of 1×10^{-3} s^{-1} at room temperature. The final data of tensile tests were based on the average result of three specimens.

2.4. Corrosion testing

An immersion test, using the weight loss of samples, was performed for 7 days in m-SBF at 37 °C. The ratio of the m-SBF solution volume (ml) to the sample surface area (cm^2) was 20 ml/cm^2. Before weighting, the corroded sample was cleaned in a solution containning 180 g/L chromic acid and 10 g/L $AgNO_3$ solution. The final data collected from the immersion tests were averaged from three different specimens.

2.5. In vivo degradation testing

Three 4-month-old male Sprague Dawley (SD) rats with body weight of 200–250 g were provided by Sixth People's Hospital affiliated to Shanghai Jiao Tong University, School of Medicine. The rats were anesthetized with 3% pentobarbital sodium and exposed through the anterolateral approach. Operation site was around the back of the rat for subcutaneous implantation. The as-cast Z2 alloy, R3-91%, and high pure Mg (99.99%) were selected for implantation (the size of sheet implants 6 × 4 × 1.5 mm). After implantation, no antibiotics were given and no infections were observed post operation. After 3 months of post-operation, these rats were sacrificed. The sheet implants were removed and then ultrasonically rinsed with a solution of 180 g/L chromic acid and 10 g/L $AgNO_3$ to remove the corrosion product around the samples. Then, all samples were cleaned with deionized water and pure ethanol. The corrosion rate of these samples was calculated from weight loss using the following formula:

$$\text{Corrosion rate } (\text{mm}/\text{year}) = \frac{k \times W}{T \times A \times D} \quad (1)$$

where k is a constant (8.76×10^4), W is the weight loss (g), T is the time exposed to solution (h), A is the surface area (cm^2) of sheet implants, and D is the density of the material (g/cm^3, for Z2 alloy and HPM, it is 1.74).

All animal experiments were conducted according to the Guidance Suggestions for the Care and Use of Laboratory Animals (issued by the Ministry of Science and Technology of the People's Republic of China) and approved by the Animal Care and Experiment Committee of Sixth People's Hospital affiliated to Shanghai Jiao Tong University, School of Medicine.

2.6. Statistical methods

The values determined in the present study were shown as mean values (three samples) and standard deviation. Statistical analysis was performed with SPSS (SPSS 16.0 Inc., Chicago, USA). One-way ANOVA and Student–Newman–Keuls post hoc tests were used to determine the level of significance for the weight loss of samples during the in vivo degradation testing. p values less than 0.05 were considered to be significant.

3. Experimental results

Fig. 1 demonstrates the microstructures of R1-20% and R1-50% observed using EBSD. The red colour represents all the grains oriented to

Table 1
The chemical composition of Z2 alloy as analyzed by Inductively Coupled Plasma Atomic Emission Spectrometry (ICP-AES). (ppmw: ppm in weight).

Element	Mg	Zn	Si	Fe	Ni	Cu	Al	Mn	Ti	Pb	Sn
Ppmw	Bal.	20000 ± 200	20 ±10	20 ±5	5 ±4	5 ±2	20 ±3	20 ±7	10 ±2	10 ±4	7 ±4

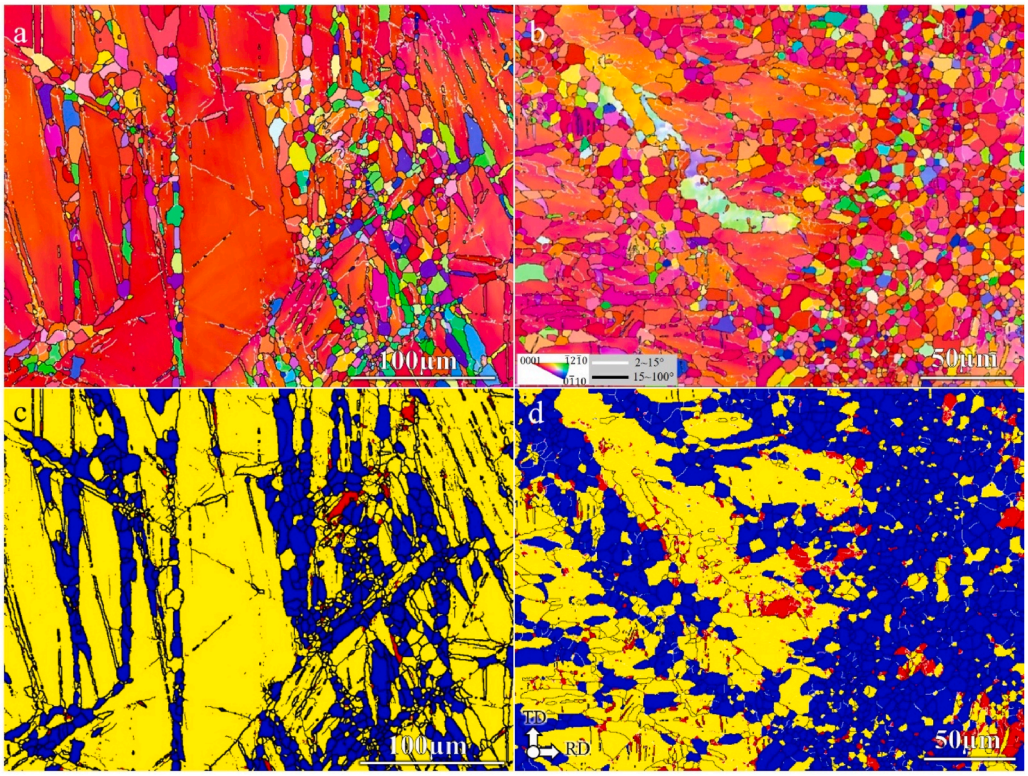

Fig. 1. EBSD inverse pole figure (IPF) maps (a, b) and images (c, d) of deformed grains (red colour), sub-grains (yellow colour) and recrystallized grains (blue colour) for R1-20% (a, c) and R1-50% (b, d).

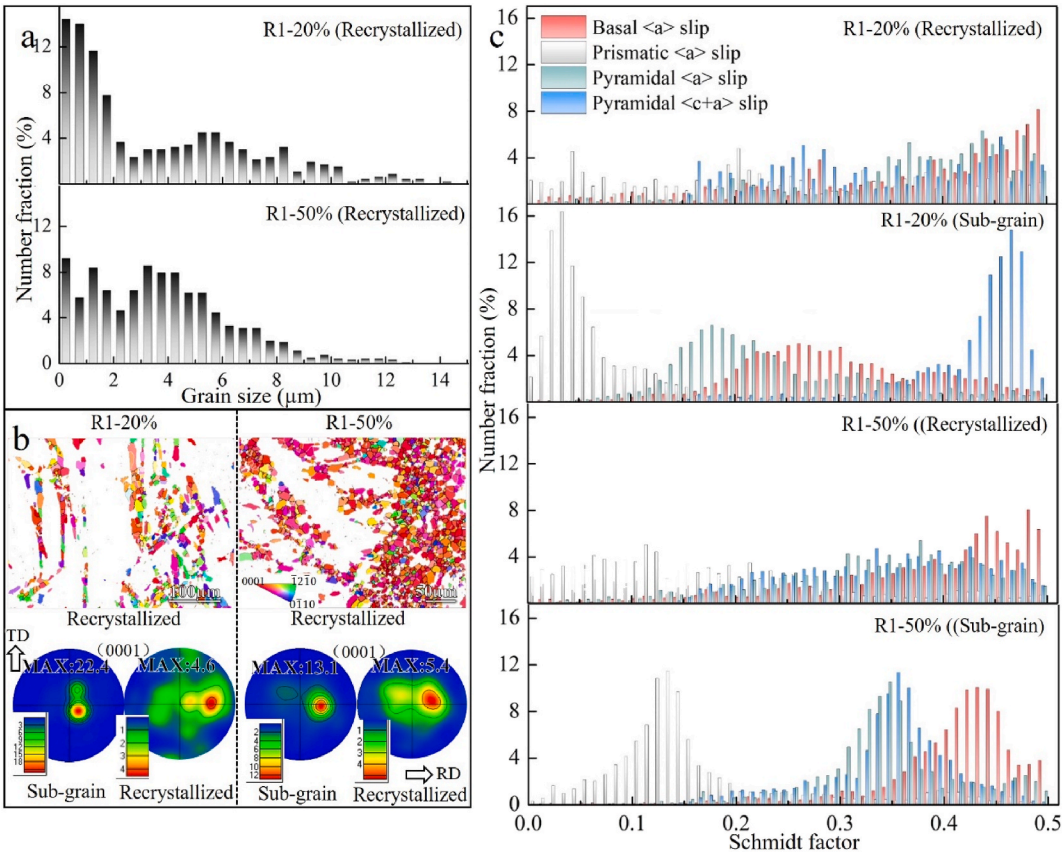

Fig. 2. (a) Grains size distribution for recrystallized grains, (b) IPF images of recrystallized grains and pole figures of recrystallized grains and sub-grains, (c) a histogram of the Schmid factor distribution for four slip systems in the recrystallized grans and sub-grains of R1-20% and R1-50%.

(0001). The c-axis of many grains is almost perpendicular to the rolling plane for both R1-20% and R1-50%, forming a strong basal texture (Fig. 1a–b). The basal texture is usually unavoidable and produced by an effect of tension twin formation and basal <a> slip during normal rolling process in most non-RE (Rare Earths) containing Mg alloys [17]. Besides, R1-20% contains a considerable amount of deformation twins, while the deformation twins were challenging to observe in R1-50%. Fig. 1c–d shows the condition of recrystallization, and the blue colour symbolizes recrystallized grains, occupying 24% and 53% area fraction in R1-20% and R1-50%, respectively. The recrystallized grains of R1-20% were mainly produced inside twins, as shown in Fig. 1c, indicating that recrystallization nucleation sites were primarily within twins, at twin-twin or twin-grain boundary intersections to form twin-induced dynamic recrystallization (TDRX) similar to other Mg alloys in recent reports [18,19]. The recrystallized grains of R1-50% seems to be the result of further recrystallization compared to R1-20%. These fine grains are much more homogeneous, and almost no twins could be observed.

Fig. 2 presents the microstructural features of the recrystallized grains and sub-grains for R1-20% and R1-50%. The grain size distribution of recrystallized grains is shown in Fig. 2a. Tiny grains (<2 μm) in R1-20% are more than those in R1-50%, while the average grain size of R1-50% is smaller than that of R1-20%. Fig. 2b displays the inverse pole figure maps of the recrystallized grains and the pole figures of the recrystallized grains and sub-grains for R1-20% and R1-50%, respectively. The texture of recrystallized grains in both R1-20% and R1-50% is similar (maximum intensity: 4.6 and 5.4). The pole figures of sub-grains express a strong basal texture. One should notice that the texture intensity of non-recrystallized grains decreased from 22.4 in R1-20% to 13.1 in R1-50%. Fig. 2c exhibits the Schmid factor for four slip systems (basal <a>, prismatic <a>, pyramidal <a> and <c+a> slips) of R1-20% and R1-50% during the rolling deformation. The two samples reveal a similar distribution of Schmid factor values in the recrystallized grains. The Schmid factor for basal slip is a little higher than the others. Nevertheless, the distribution of the Schmid factor in sub-grains demonstrates a significant difference between R1-20% and R1-50%. For R1-20% only the pyramidal <c+a> slip is reaching at relatively high values for the sub-grains. However, for R1-50% all slip systems except for the prismatic slip reach relatively high values for the sub-grains especially the basal slip.

Fig. 3 presents the microstructure of the R2-75% which was obtained after a second rolling pass of R1-50%. The grains are more homogeneous, and the average grain size is about 3.5 μm in R2-75%. A robust basal texture with a maximum intensity of 12 was formed, and most of the grains are recrystallized as shown in Fig. 3c. Fig. 3d demonstrates the Schmid factor for four slip systems of R2-75%. Only pyramidal <c+a> slip systems show the high Schmid factor values.

Fig. 4 displays the TEM images of the microstructures of R1-50% and R2-75%. The GBs of R1-50% are irregular (Fig. 4a). Moreover, Zn segregation at GBs shows more brightly than Mg matrix, observing in the HAADF-STEM image, as shown in Fig. 4b. The grains of R2-75% are tiny and relatively uniform (Fig. 4c), which was achieved due to sufficient recrystallization after the second pass of hot rolling. Likewise, GBs segregations still can be detected in R2-75%, as shown in Fig. 4d.

The TEM images of the microstructure of R3-91% after the third rolling pass performed on R2-75% is shown in Fig. 5. The grains are very tiny, and just a very few grains were over 100 nm (Fig. 5a). The corresponding selected area electron diffraction (SAED) pattern reveals continuous diffraction rings indicating the random orientations of nanocrystalline phase with high angle GBs. Fig. 5b–c exhibits the bright and dark-field STEM images for a better view of the nanocrystals. The average grain size of R3-91% is about 70 nm (measured by Nano Measurer software). In recent similar studies, large-strain hot rolling (three passes with total reduction 85%) [20] and accumulative roll bonding (80% in one pass) [21] could only refine the grain size to about 1–3 μm in AZ61alloy. Fig. 5d confirms also the GB segregation by Zn

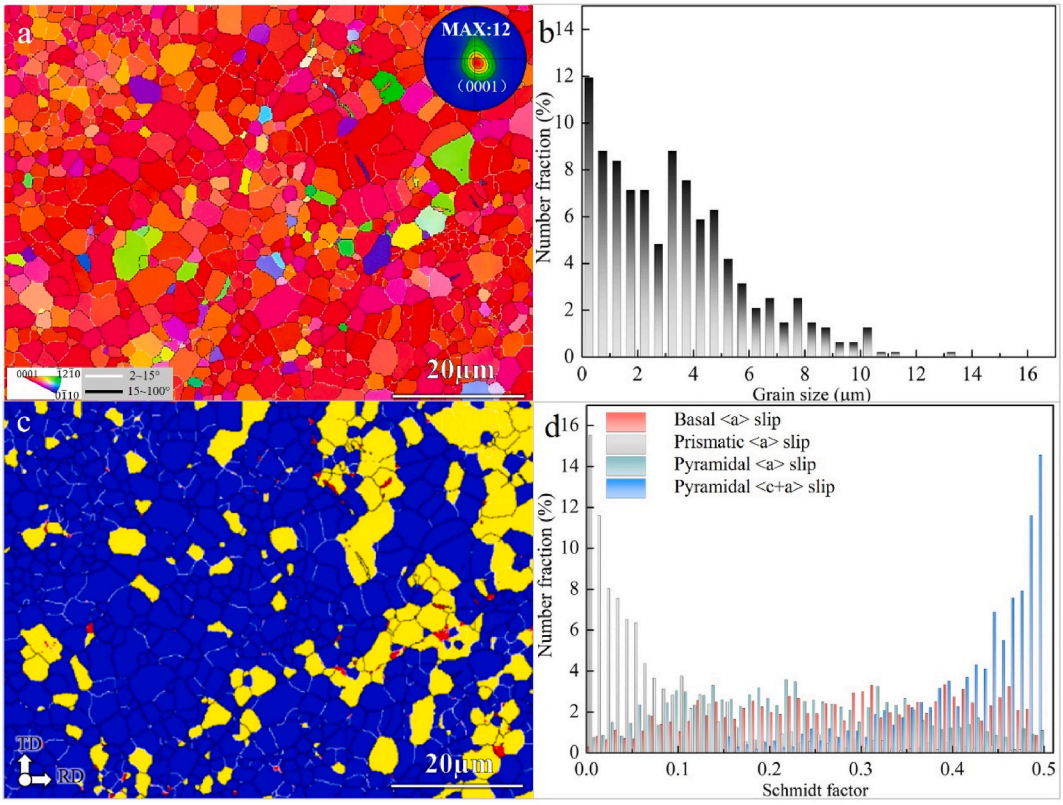

Fig. 3. (a) IPF images of recrystallized grains and pole figures, (b) grains size distribution for Fig. 2a, (c) images of deformed grains (red colour), sub-grains (yellow colour) and recrystallized grains (blue colour), (d) a histogram of the Schmid factor distribution of four slip systems for R2-75%.

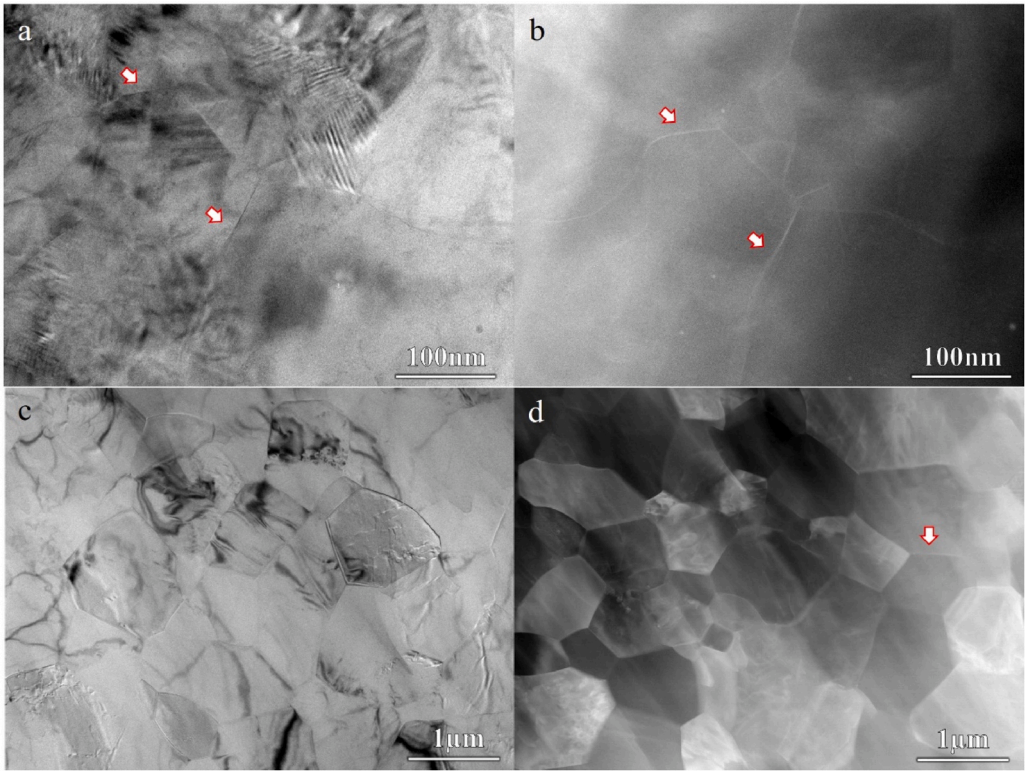

Fig. 4. (a) Bright-field TEM and (b) HAADF-STEM image of R1-50%. (c) Bright-field TEM and (d) ADF-STEM image of R2-75%.

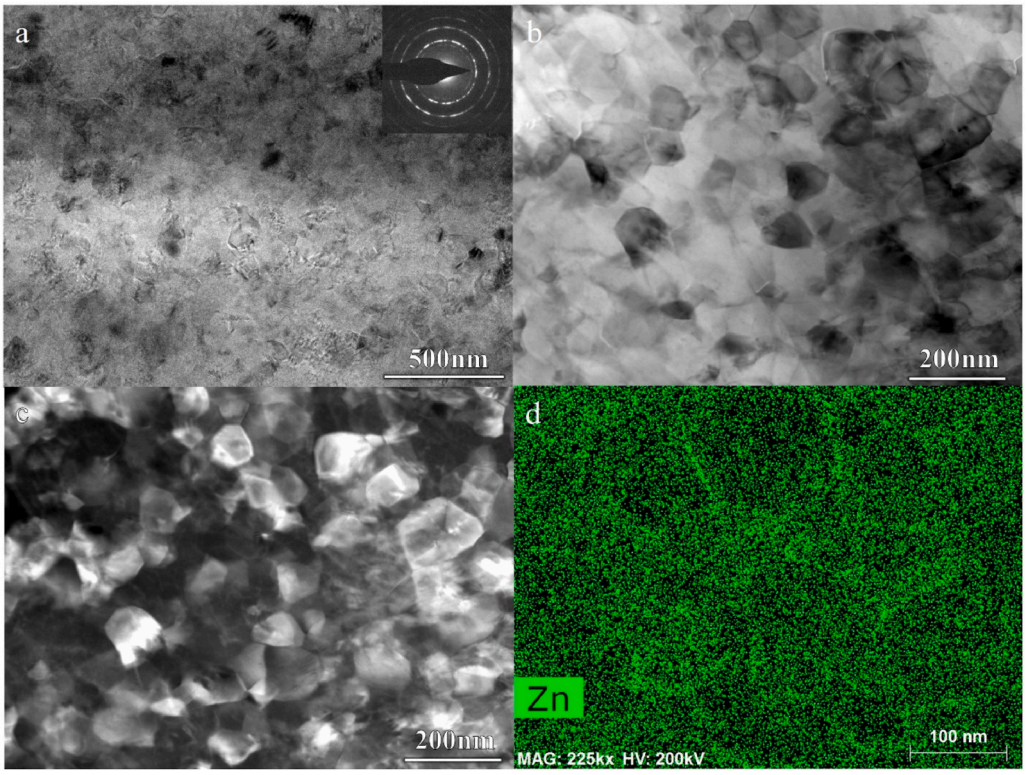

Fig. 5. (a) Bright-field TEM, (b) bright-field STEM, and (c) dark-field STEM image of R3-91%. (d) EDX mapping of Zn segregations. Insert in (a) is the selected area electron diffraction of this area (SAED).

atoms in R3-91%, as already observed in R1-50% and R2-75%. This segregation behaviour was also detected in the Mg–2Zn alloy after single passed rolling with 80% reduction in a previous study [22].

Fig. 6a summarizes the mechanical properties, and corrosion resistance of as-cast and all rolled Z2 samples. Compared with the as-cast material, the yield strength (YS) and elongation of R1-20% were

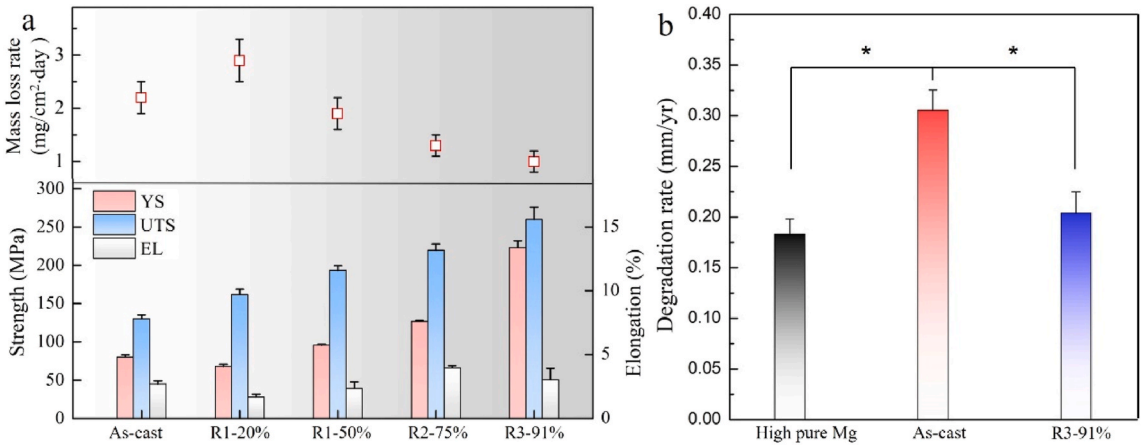

Fig. 6. (a) Corrosion rates (immersion in m-SBF solution at 37 °C with one week) and tensile properties of Z2 alloy with different rolling processes. (b) In vivo degradation rate of high pure Mg, as-cast Z2 alloy, and R3-91% during subcutaneous implantation with three months in SD rat. *p < 0.05.

decreasing, indicating that R1-20% with a high fraction of twins was more susceptible to shear localization and fracture. With the increase of rolling reduction and rolling passes, the YS and ultimate tensile stress (UTS) of R1-50%, R2-75%, and R3-91% raised rapidly, while the elongation was fluctuating. Finally, the yield strength (YS) and ultimate tensile strength (UTS) reached 223 MPa and 260 MPa, respectively, in R3-91%. The values of mass loss rate as a function of rolling passes and reduction of Z2 alloy within 1-week immersion in m-SBF solution at 37 °C were about 2.2, 2.9, 1.9, 1.3 and 1.0mg/cm^{2}day, respectively. Since the mass loss is equivalent to the amount of Mg dissolved in the anodic reaction, this result suggests that the R3-91% has the best corrosion resistance. Fig. 6b shows the results further to evaluate the in vivo degradation rate of R3-91%. The average degradation rate of R3-91% was 0.2 mm/year during implantation with three months in SD rat, which was similar to that of high purity Mg. Fig. 7 shows the in vivo corrosion morphology of high pure Mg, as-cast Z2 alloy, and R3-91% during subcutaneous implantation with 3 months in SD rat. The degradation products of HPM surface are thinner than that of Z2 alloys. In addition, degradation product film in as-cast Z2 alloy is porous in comparison with the surface film of R3-91% (Fig.7 b, e, h). After removing degradation products, it is obvious that the corrosion attacked in the matrix of as-cast Z2 alloy is most serious (Fig. 7 f). The HPM and

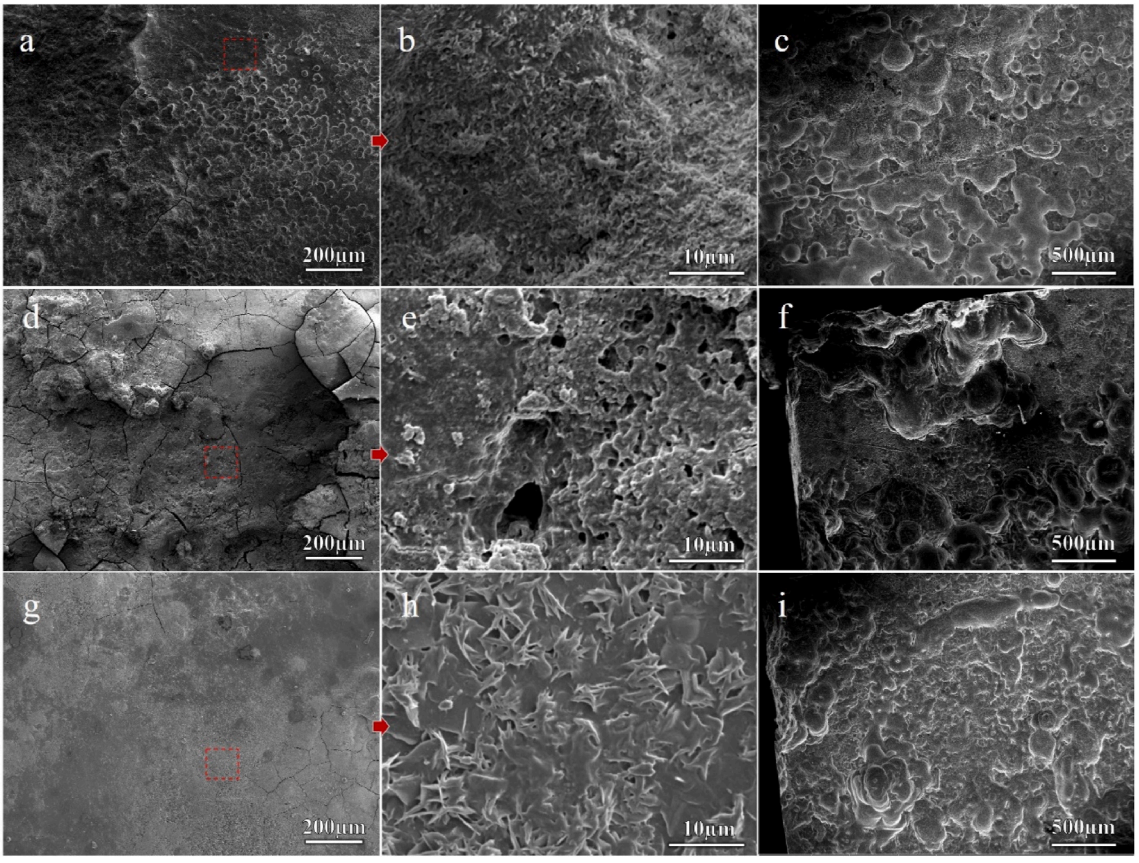

Fig. 7. (a) In vivo corrosion morphology (figures c, f and i are without degradation products) of high pure Mg (a, b and c), as-cast Z2 alloy (d, e, f), and R3-91% (g, h and i) during subcutaneous implantation with 3 months in SD rat.

R3-91% have a slight local corrosion. Fig. 8 represents the chemical composition of degradation products formed on high pure Mg, as-cast Z2 alloy, and R3-91% after the implantation. Compositional analysis based on SEM and EDS demonstrates that Ca and P could be detected in degradation products, expressing insoluble degradation products such as different types of (Mg/Ca) phosphate or carbonate tend to precipitate on the surface of the implant. It is also noteworthy that the Zn content in the degradation product is a little higher (2 at.%) than that in the matrix (0.7 at.%) in the R3-91% sample. The degradation layers with about 100 mm thickness can slow down corrosion, decrease local alkalization, thus finally influence cell attachment to the implantation surface by changing the surface chemical activity and morphology in these samples.

4. Discussion

The application of biodegradable Mg requires high strength, low corrosion rate, and proper biosafety. Usually, even though precipitates can significantly improve strength, they can also increase the corrosion rate of Mg through micro-galvanic corrosion [23,24]. Also, residual micro-strain and dislocations in deformed grains and deformation twin harm corrosion resistance [22,25]. The microstructure needs a single α-Mg phase with few dislocations and residual strain to avoid a low corrosion resistance. Thus, only grain refinement is an effective way to achieve both high strength and favourable corrosion resistance [26]. Therefore, the nanocrystalline Z2 alloy with single α-Mg phase was developed with superior high yield strength and relative low corrosion rate by multiple hot rolling steps (Fig. 6).

Due to the hcp crystal structure with high anisotropy, Mg shows a complex deformation behaviour. The (0001) $<11\bar{2}0>$ basal slip is known to be the easiest system to be activated at all temperatures [27]. The other potential slip systems are $(10\bar{1}0)$ $<\bar{1}2\bar{1}0>$ prismatic slip, $(10\bar{1}1)$ $<\bar{1}2\bar{1}0>$ pyramidal slip, and $(11\bar{2}2)$ $<\bar{1}\bar{1}23>$ pyramidal slip (<c+a> slip) [28]. The main twinning systems are tension twinning $\{10\bar{1}2\}$ and compressive twinning $\{10\bar{1}1\}$ [28]. Non-basal slip systems are very temperature-dependent and only observed at higher temperatures (>180 °C) [29]. In this study, the nanocrystalline R3-91% was obtained under hot rolling at 400 °C after three passes. Every pass of rolling exceeded 50% reduction with a large strain accommodated by different deformation mechanism. During the first rolling pass with 20% reduction, basal <a> slip and tension twining, which are the easiest to be activated, dominated the deformation mechanism. Both of them resulted in orientation of the c axis of grains perpendicular to the rolled surface, forming a strong basal texture (Fig. 1a) [17]. At the same time, TDRX, which produced fine recrystallized grains with random orientation, controlled grain refinement (Fig. 1c). Thus, the orientation of these fine recrystallized grains deviated from the basal texture. The parental (untwined) grains with coarse size formed sub-grains or deformed grains and remained in basal texture in R1-20%. In subsequent rolling deformation (R1-20% to R1-50%), compressive twinning and pyramidal <c+a> slip were activated, and accommodated the plastic deformation with basal slip, providing further TDRX in the parental grains. The Schmid factor for pyramidal <c+a> slip was obviously larger than for the other slip systems, and the compressive twinning was activated when the c axis of grains was under compression (Fig. 2c) [30]. Besides, the critical resolved sheer stress (CRSS) for compressive twinning depends on temperature and decreases considerably at 400 °C [27]. Above discussion is illustrated in a schematic diagram for better visualization (Fig. 9a–b).

When the rolling reduction increased to 50% during the first rolling pass (Fig. 9b–c), the recrystallized grains, which originated from the residual coarse grains of R1-20%, increased significantly through further TDRX. Accordingly, these new recrystallized grains in R1-50% and R1-20% have similar features, including grain size distribution and orientation. However, the previously recrystallized grains in R1-20% also underwent the deformation during the rolling reduction of 20%–50%. Since the Schmid factor for the four slip systems is similar, the basal slip with the least CRSS was dominating the deformation mechanism in these recrystallized grains, resulting in a rotation of the c axis to ND after 50% reduction of rolling. Therefore, the peak of the pole figure for recrystallized grains rotates towards to (0001) from R1-20% to R1-50% (Fig. 2b). Besides, twinning could not be activated in these fine recrystallized grains. The critical grain size for twinning is 2.7 μm for pure Mg at room temperature [31] and increases significantly with temperature. Below the critical grain size, dislocation slip is expected to be favourable.

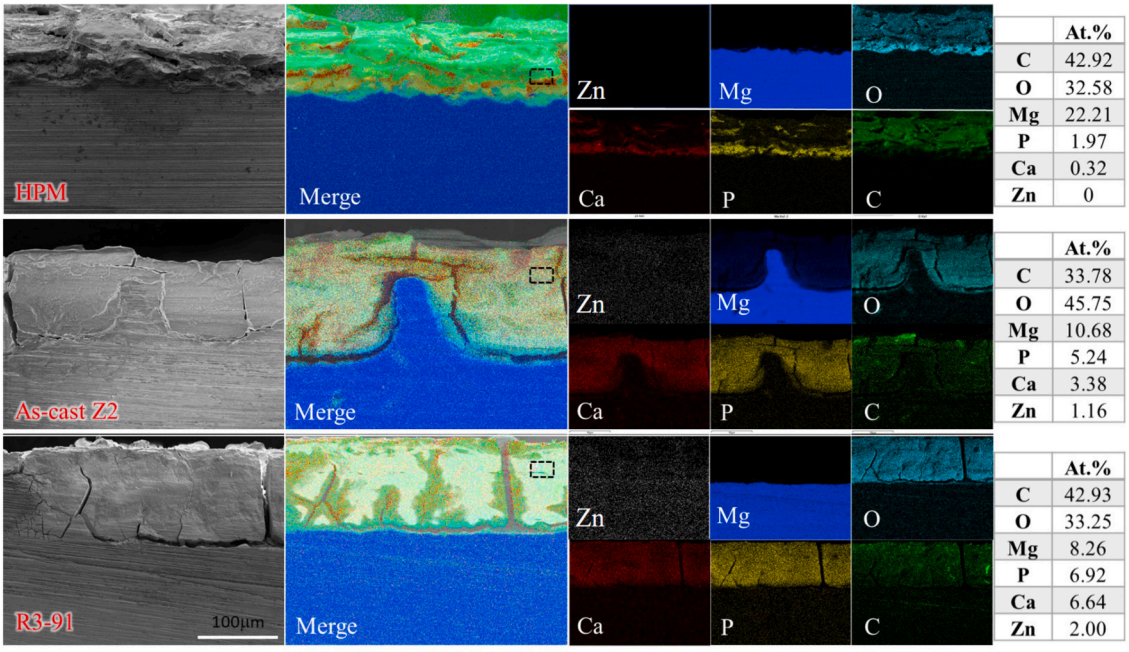

	At.%
C	42.92
O	32.58
Mg	22.21
P	1.97
Ca	0.32
Zn	0

	At.%
C	33.78
O	45.75
Mg	10.68
P	5.24
Ca	3.38
Zn	1.16

	At.%
C	42.93
O	33.25
Mg	8.26
P	6.92
Ca	6.64
Zn	2.00

Fig. 8. Cross sectional images of the in vivo corrosion products of the high purity Mg, as-cast Z2 alloy, and R3-91% during subcutaneous implantation with 3 months in SD rat and corresponding elemental mappings.

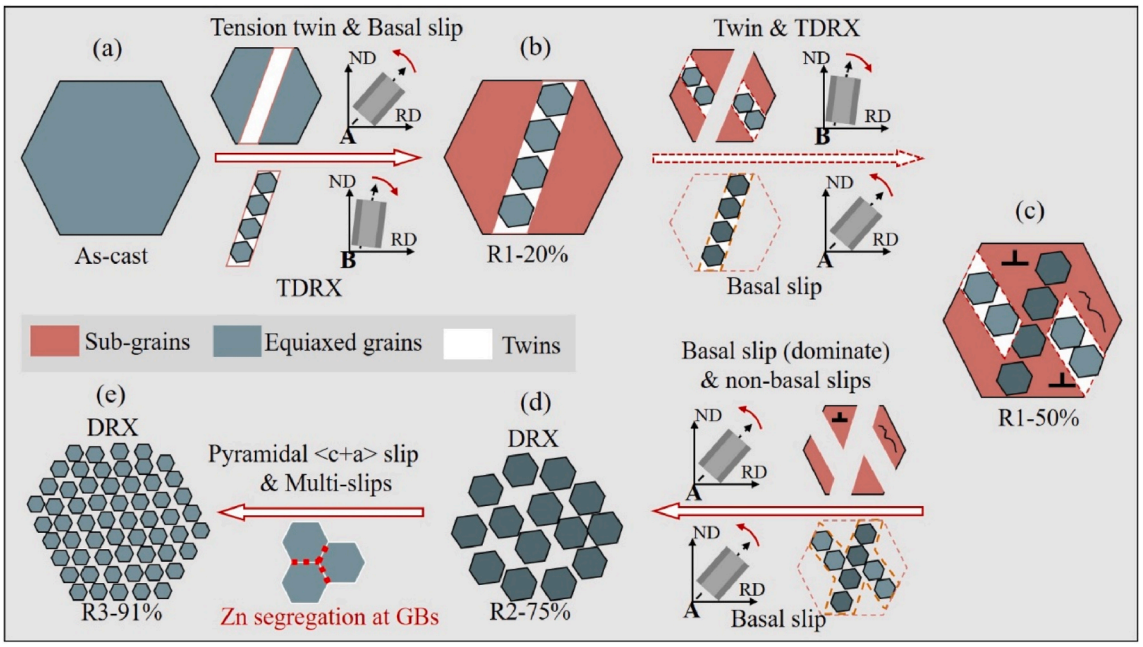

Fig. 9. Schematic diagram for grains refinement of Z2alloy during hot rolling processes.

During the second rolling pass (Fig. 9c–d), the sub-grains (coarse grains) and the recrystallized grains (fine grains) in R1-50% expressed different deformation behaviour due to their Schmid factor difference and grain size effect. Firstly, recrystallized grains with small grain size have a higher deformation resistance than sub-grains. Secondly, the Schmid factor for the four slip systems is similar in recrystallized grains, and the basal slip dominates the deformation mechanism. Nevertheless, except of basal slip, the pyramidal <a> and <c+a> slip are also with a high Schmid factor in the sub-grains of R1-50% (Fig. 2c). Thus, under the synergistic effects of basal and non-basal slips, the sub-grain dynamic recrystallization (DRX) occurred, resulting in further grain refinement. Thus, after the second rolling pass, the R2-75% formed uniform fine grains, and the strong basal texture is the result of the domination of basal slip (Fig. 3a).

Finally, the third rolling pass performed on R2-75% produced the intended nanocrystalline microstructure in R3-91% (Fig. 9d–e). During this process, the (a+c) dislocations are required for the formation of three-dimensionally distributed recrystallization nuclei and high-angle grain boundaries to produce nanocrystals. The activation of pyramidal <c+a> slip was observed at 150 °C for ZK60 alloy [32] and for Mg-3wt.%Y alloy at room temperature [33]. Here, three factors can promote the activation of pyramidal <c+a> slip in R2-75%. Firstly, the high temperature decreased CRSS of pyramidal <c+a> slip. The CRSS of pyramidal <c+a> slip is similar to prismatic slip and below 10 MPa in Mg single crystal at 400 °C [34]. Secondly, small grain size requires high stress, which in turn activates pyramidal <c+a> slip [35]. The average grain size was about 3.5 μm in R2-75%, providing relatively high stress. Finally, the strong basal texture leads to a huge Schmid factor for pyramidal <c+a> slip in R2-75% (Fig. 3a and d). According to the Schmid law requires [29].

$$\sigma \cdot m = \tau_{pyra} \quad (2)$$

where σ is the applied stress and τ is the CRSS for pyramidal <c+a> slip, and m is the Schmid factor. Therefore, high temperature (τ_{pyra} ↓), small grain size (σ ↑), and strong basal texture (m ↑) contribute to the activation of pyramidal <c+a> slip according to the above equation. Three-dimensional recrystallization nuclei formed nanocrystals under the influence of pyramidal <c+a> and basal slip under continuous plastic deformation with a large strain. Besides, segregation of Zn atoms at GBs were observed in R1-50%, R2-75%, and R3-91%, which always accompanies the processes of grain refinement during the whole rolling passes for R3-91%. This segregation behaviour is significant for the formation of nanocrystals. First of all, Zn segregation can harden GBs and restrain GB sliding [36], especially at high temperature, providing more dislocation slips for DRX during the rolling processes. Secondly, GB segregation can restrain its growth, lowering the GB energy and bring the system closer to thermodynamic equilibrium, thereby dramatically enhancing nanocrystals stability [37]. Finally, homogeneous nanocrystals were achieved through the synergetic effects of deformation mechanisms and microstructural features during the hot rolling process of Z2 alloy.

In most Mg alloys, it was almost impossible to promote overall performance including strength and corrosion resistance, and biocompatibility for biomedical by adding alloy elements. Some researchers and companies had to choose HPM without any alloying elements for clinical application to ensure biosafety and a stable degradation, although scarified the mechanical property [38]. In present work, the novel lean alloy of bulk Z2 with particular nanocrystals could coordinate the contradiction among strength, corrosion resistance, and biocompatibility. The raw material is cheap and abundant, and the preparation technology was simple and efficient. Under further research, the lean nanocrystalline Mg alloy was quite hopeful to be as biomedical devices for clinical application.

5. Conclusion

Nanograins (about 70 nm) with Zn segregation at their GBs were successfully produced in a lean biodegradable Z2 alloy via hot rolling with three rolling process. The nanocrystalline Z2 alloy demonstrates a high strength (223 MPa (YS) and 260 MPa (UTS)) and good corrosion resistance. At the first rolling stages, TDRX dominated the grain refinement of coarse grains. During the last rolling pass, the created sample microstructure and rolling parameters meet the condition for the activation of pyramidal <c+a> slip, and multi-slips dominated the deformation mechanism and DRX to form the nanocrystals rounded by Zn atoms final microstructure.

CRediT authorship contribution statement

Wenhui Wang: Conceptualization, Investigation, Visualization, Writing – original draft, Writing – review & editing. **Carsten Blawert:** Supervision, Writing – review & editing. **Rui Zan:** Visualization. **Yu Sun:** Visualization. **Hongzhou Peng:** Visualization. **Jiahua Ni:** Conceptualization. **Tao Suo:** Visualization. **Yang Song:** Conceptualization. **Shaoxiang Zhang:** Conceptualization. **Mikhail L. Zheludkevich:** Supervision, Writing – review & editing. **Xiaonong Zhang:** Supervision, Writing – review & editing.

Declaration of competing interest

The authors declare that they have no known competing financial interests or personal relationships that could have appeared to influence the work reported in this paper.

Acknowledgements

This work was funded by the National Key R&D Program of China (No.2018YFC1106600), and the "Science and Technology Innovation 2025" Major Special Project of Ningbo (No.2019B10064). Wenhui Wang thanks the China Scholarship Council (CSC) for the award of fellowship and funding. Thanks for the technology support by Ying Zhang, Yunting Li and Xiaomin Li from Instrumental Analysis Center, Shanghai Jiao Tong University.

References

[1] D. Zhao, F. Witte, F. Lu, J. Wang, J. Li, L. Qin, Current status on clinical applications of magnesium-based orthopaedic implants: a review from clinical translational perspective, Biomaterials 112 (2017) 287–302.
[2] Y. Zheng, X. Gu, F. Witte, Biodegradable metals, Materials Science and Engineering: R. Rep. 77 (2014) 1–34.
[3] Y. Zhang, J. Xu, Y.C. Ruan, M.K. Yu, M. O'Laughlin, H. Wise, D. Chen, L. Tian, D. Shi, J. Wang, S. Chen, J.Q. Feng, D.H. Chow, X. Xie, L. Zheng, L. Huang, S. Huang, K. Leung, N. Lu, L. Zhao, H. Li, D. Zhao, X. Guo, K. Chan, F. Witte, H. C. Chan, Y. Zheng, L. Qin, Implant-derived magnesium induces local neuronal production of CGRP to improve bone-fracture healing in rats, Nat. Med. 22 (2016) 1160–1169.
[4] X. Li, K. Lu, Playing with defects in metals, Nat. Mater. 16 (2017) 700–701.
[5] X. Li, K. Lu, Improving sustainability with simpler alloys, Science 364 (2019) 733–734.
[6] Y. Li, C. Wen, D. Mushahary, R. Sravanthi, N. Harishankar, G. Pande, P. Hodgson, Mg–Zr–Sr alloys as biodegradable implant materials, Acta Biomater. 8 (2012) 3177–3188.
[7] W.H. Wang, D. Wu, R.S. Chen, X.N. Zhang, Effect of solute atom concentration and precipitates on serrated flow in Mg-3Nd-Zn alloy, J. Mater. Sci. Technol. 34 (2018) 1236–1242.
[8] R.Z. Valiev, Nanostructuring of metals by severe plastic deformation for advanced properties, Nat. Mater. 3 (2004) 511–516.
[9] L.G. Sun, G. Wu, Q. Wang, J. Lu, Nanostructural metallic materials: structures and mechanical properties, Mater. Today 38 (2020) 114–135.
[10] Z. Pu, G.L. Song, S. Yang, J.C. Outeiro, O.W. Dillon, D.A. Puleo, I.S. Jawahir, Grain refined and basal textured surface produced by burnishing for improved corrosion performance of AZ31B Mg alloy, Corrosion Sci. 57 (2012) 192–201.
[11] F.L. Nie, Y.F. Zheng, S.C. Wei, D.S. Wang, Z.T. Yu, G.K. Salimgareeva, A. V. Polyakov, R.Z. Valiev, In vitro and in vivo studies on nanocrystalline Ti fabricated by equal channel angular pressing with microcrystalline CP Ti as control, J. Biomed. Mater. Res. 101A (2013) 1694–1707.
[12] P. Minárik, J. Veselý, R. Král, J. Bohlen, J. Kubásek, M. Janeček, J. Stráská, Exceptional mechanical properties of ultra-fine grain Mg-4Y-3RE alloy processed by ECAP, Mater. Sci. Eng., A 708 (2017) 193–198.
[13] P. Serre, R.B. Figueiredo, N. Gao, T.G. Langdon, Influence of strain rate on the characteristics of a magnesium alloy processed by high-pressure torsion, Mater. Sci. Eng. 528 (2011), 3601-2608.
[14] R.Z. Valiev, R.K. Islamgaliev, I.V. Alexandrov, Bulk nanostructured materials from severe plastic deformation, Prog. Mater. Sci. 45 (2000) 103–189.
[15] S. Zhang, X. Zhang, C. Zhao, J. Li, Y. Song, C. Xie, H. Tao, Y. Zhang, Y. He, Y. Jiang, Y. Bian, Research on an Mg-Zn alloy as a degradable biomaterial, Acta Biomater. 6 (2010) 626–640.
[16] J. Li, Y. Song, S. Zhang, C. Zhao, F. Zhang, X. Zhang, L. Cao, Q. Fan, T. Tang, In vitro responses of human bone marrow stromal cells to a fluoridated hydroxyapatite coated biodegradable Mg-Zn alloy, Biomaterials 31 (2010) 5782–5788.
[17] D. Griffiths, Explaining texture weakening and improved formability in magnesium rare earth alloys, Mater. Sci. Technol. 31 (2015) 10–24.
[18] S.H. Lu, D. Wu, R.S. Chen, E.-H. Han, Reasonable utilization of {10-12} twin for optimizing microstructure and improving mechanical property in a Mg-Gd-Y alloy, Mater. Des. 191 (2020) 108600.
[19] I. Basu, T. Al-Samman, Twin recrystallization mechanisms in magnesium-rare earth alloys, Acta Mater. 96 (2015) 111–132.
[20] J.A. del Valle, M.T. Pérez-Prado, O.A. Ruano, Texture evolution during large-strain hot rolling of the Mg AZ61 alloy, Mater. Sci. Eng., A 355 (2003) 68–78.
[21] J.A. del Valle, M.T. Pérez-Prado, O.A. Ruano, Accumulative roll bonding of a Mg-based AZ61 alloy, Mater. Sci. Eng., A 410–411 (2005) 353–357.
[22] W. Wang, H. Wu, R. Zan, Y. Sun, C. Blawert, S. Zhang, J. Ni, M.L. Zheludkevich, X. Zhang, Microstructure controls the corrosion behavior of a lean biodegradable Mg–2Zn alloy, Acta Biomater. 107 (2020) 349–361.
[23] J. Chen, L. Tan, K. Yang, Recent advances on the development of biodegradable magnesium alloys: a review, Mater. Technol. 31 (2016) 681–688.
[24] Y. Zheng, Y. Li, J. Chen, Z. Zou, Effects of tensile and compressive deformation on corrosion behaviour of a Mg–Zn alloy, Corrosion Sci. 90 (2015) 445–450.
[25] W.H. Wang, H.L. Wu, Y. Sun, J. Yan, L. Zhang, S.X. Zhang, J.H. Ni, Y. Song, X. N. Zhang, Local intragranular misorientation accelerates corrosion in biodegradable Mg, Acta Biomater. 101 (2020) 575–585.
[26] K.D. Ralston, N. Birbilis, Effect of grain size on corrosion A Review, Corrosion 66 (2010), 075005.
[27] A. Chapuis, J.H. Driver, Temperature dependency of slip and twinning in plane strain compressed magnesium single crystals, Acta Mater. 59 (2011) 1986–1994.
[28] Y. Gan, W. Song, J. Ning, Crystal plasticity analysis of plane strain deformation behavior and texture evolution for pure magnesium, Comput. Mater. Sci. 123 (2016) 232–243.
[29] S.R. Agnew, Ö. Duygulu, Plastic anisotropy and the role of non-basal slip in magnesium alloy AZ31B, Int. J. Plast. 21 (2005) 1161–1193.
[30] M.R. Barnett, Twinning and the ductility of magnesium alloys, Mater. Sci. Eng., A 464 (2007) 1–16.
[31] H. Fan, S. Aubry, A. Arsenlis, J.A. El-Awady, Grain size effects on dislocation and twinning mediated plasticity in magnesium, Scripta Mater. 112 (2016) 50–53.
[32] A. Galiyev, R. Kaibyshev, G. Gottstein, Correlation of plastic deformation and dynamic recrystallization in magnesium alloy ZK60, Acta Mater. 49 (2001) 1199–1207.
[33] S. Sandlöbes, S. Zaefferer, I. Schestakow, S. Yi, R. Gonzalez-Martinez, On the role of non-basal deformation mechanisms for the ductility of Mg and Mg-Y alloys, Acta Mater. 59 (2011) 429–439.
[34] T. Obara, H. Yoshinga, S. Morozumi, {112¯2}⟨1123⟩ Slip system in magnesium, Acta Metall. 21 (1973) 845–853.
[35] B.-Y. Liu, F. Liu, N. Yang, X.-B. Zhai, L. Zhang, Y. Yang, B. Li, J. Li, E. Ma, J.-F. Nie, Z.-W. Shan, Large plasticity in magnesium mediated by pyramidal dislocations, Science 365 (2019) 73–75.
[36] J. Hu, Y.N. Shi, X. Sauvage, G. Sha, K. Lu, Grain boundary stability governs hardening and softening in extremely fine nanograined metals, Science 355 (2017) 1292–1296.
[37] Z.B. Jiao, C.A. Schuh, Nanocrystalline Ag-W alloys lose stability upon solute desegregation from grain boundaries, Acta Mater. 161 (2018) 194–206.
[38] Yu Sun, Hongliu Wu, Wenhui Wang, Rui Zan, Hongzhou Peng, Shaoxiang Zhang, Xiaonong Zhang, Translational status of biomedical Mg devices in China, Bioactive Materials 4 (2019) 358–365.